Gigagauss-scale quasistatic magnetic field generation in a snail-shaped target

Ph. Korneev*
NRNU MEPhI, Moscow 115409, Russian Federation and University of Bordeaux, CNRS, CEA, CELIA, 33405 Talence, France

E. d'Humières and V. Tikhonchuk
University of Bordeaux, CNRS, CEA, CELIA, 33405 Talence, France

(Received 30 September 2014; revised manuscript received 25 December 2014; published 22 April 2015)

A simple setup for the generation of ultra-intense quasistatic magnetic fields, based on the generation of electron currents with a predefined geometry in a curved snail (or 'escargot') target, is proposed and analyzed. Particle-in-cell simulations and qualitative estimates show that gigagauss scale magnetic fields may be obtained with existent laser facilities. The described mechanism of the strong magnetic field generation may be useful in a wide range of applications, from laboratory astrophysics to magnetized inertial confinement fusion schemes.

DOI: 10.1103/PhysRevE.91.043107 PACS number(s): 52.25.Xz, 52.38.Fz, 52.55.Ez, 52.65.Rr

I. INTRODUCTION

The generation of strong magnetic fields in laboratory conditions attracts much interest as it may be used in various applications, such as astrophysical studies, Inertial Confinement Fusion (ICF) schemes, magnetic field interaction with atoms and particles, etc. For the laboratory production of magnetic fields of the order of hundreds of kilogauss, pulsed magnetic sources can be used. Nowadays, laser facilities provide new possibilities for the one-shot generation of intense magnetic fields up to tens of megagauss, in a volume $\lesssim 0.1\ \mathrm{mm}^3$ in a nanosecond time scale [1–3].

Here we propose a novel scheme for production of intense magnetic fields, based on the generation of intense currents in a target of a special 'escargot' geometry [4,5]. The scheme can be understood from Fig. 1(A1), where a laser pulse propagates inside the target from the left through the 'window'. As a result of a grazing incidence and the target geometry, various physical phenomena are involved into the interaction process. We mention here the laser pulse reflection from plasma, the electron surface guiding effect [6], and the return current generation. A combination of these three effects in the considered target geometry results in a strong magnetic field generation. A curvature of the inner target surface provides (i) a continuous laser propagation along the surface and a high total absorption, (ii) an acceleration of electrons along the curved target surface, (iii) a return current with a target-defined curvature. The electron guiding along the target inner surface (ii), known as the electron surface acceleration mechanism, is described in [6]. The effect was experimentally confirmed [7], for laser intensities $\sim 10^{18}\mathrm{W/cm}^2$, and studied numerically in different geometries [6,8]. It was found that the accelerated electrons produce strong currents along the surface, with the corresponding magnetic fields. Another important phenomena, not mentioned in [4], is the return current generation (iii) in a target material. It results in the generation of a quasistatic magnetic field of the opposite direction. The field amplitude may reach a gigagauss level, with the characteristic lifetime of the order of at least several ps. This quasistationary magnetic field may deflect the surface electron guiding, and, moreover, produce highly magnetized electron off-surface flows. In this paper, with particle-in-cell simulations we show an example of gigagauss scale magnetic field generation and analyze the physical origin of this effect.

The paper is organized as follows. First, we present the results of the particle-in-cell simulations, then discuss the magnetic field structure and its origin, and finally conclude. We use relativistic units throughout the paper and in figures, if it is not explicitly written.

II. PARTICLE-IN-CELL SIMULATIONS FOR AN EXAMPLE OF THE MAGNETIC FIELD GENERATION IN AN 'ESCARGOT' TARGET

To produce a strong curved solenoid-like current, a special snail, or 'escargot' target geometry is proposed, see Fig. 1(A1). Our simulations are two dimensional, so the real 3D shape of the target is somewhat like a disclosed deformed cylinder. This geometry allows us to make use of the plasma mirror effect [10], with a mirror of a prescribed geometry, and to predefine the currents directions. The discontinuity of the target is necessary for the propagation of the laser pulse inside. The target shape is analytically defined by

$$r(\theta) = r_0\left(1 + \frac{\delta r}{r_0}\frac{\theta}{2\pi}\right), \quad \theta \in (0, 2\pi), \tag{1}$$

where $\theta = 0$ corresponds to the upper direction of the vertical axis in Fig. 1, δr and r_0 are the parameters, defined below. We simulate the laser-target interaction with 2D3V particle-in-cell code PICLS [11].

Below, we describe in details only one example of a Gold-type target,[1] from a set of simulations, since all of them give qualitatively the same results. The laser intensity is $I_0 = 5 \times 10^{19}\ \mathrm{W/cm}^2$, the laser wavelength $\lambda_0 = 0.93\ \mu\mathrm{m}$, and the pulse duration $\tau_0 = 1.6\,\mathrm{ps}$. The target, defined by Eq. (1), with $r_0 = 43\,\mu\mathrm{m}$ and $\delta r = 28\ \mu\mathrm{m}$, is composed of two layers of a material with the ion charge $Z = 79$, the ion mass $m_i^{(1)} = 197 m_p$ (m_p is the proton mass) of the inner $1\ \mu\mathrm{m}$ width layer, and $m_i^{(2)} = 20 m_i^{(1)}$ of the outer $2\ \mu\mathrm{m}$ width layer

*korneev@theor.mephi.ru

[1]For another example see Supplemental Material [12].

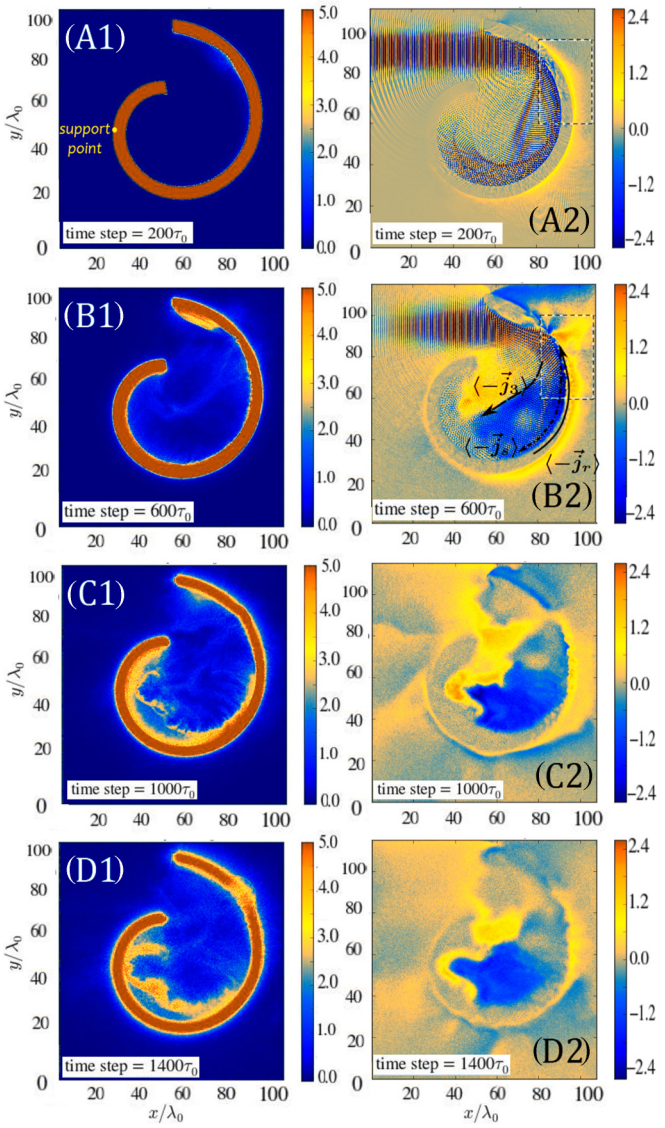

FIG. 1. (Color online) Electron density (A1–D1), and magnetic field B_z (A2–D2) at time moments: 0.62,1.9,3.1,4.3 ps correspondingly for A1,B1,C1,D1 and A2,B2,C2,D2, for the example Gold-type target. Electron density is shown in units of $n_c = 1.3 \times 10^{21}$ cm^{-3}, and is cut on the value of 6.5×10^{21} cm^{-3}. The magnetic field is shown in units of 1.16×10^8 Gauss, so that maximum value of 2.6 in the color bar corresponds to 3×10^8 Gauss. Axis z is directed to the viewer. In B2, the black dashed arrow along the target inner surface indicates surface guided electrons, the black solid arrow corresponds to the electrons, which produce reverse current, and the long-dashed arrow shows electron motion, which is deflected by the magnetic field, already formed inside the target. For the time evolution see Supplemental Material [9].

(sublayer). The ion density is $n_i = 2 \times 10^{20}$ cm^{-3}. Electrons with masses m_e have the density $n_e = Zn_i = 12n_c$, where $n_c = 1.3 \times 10^{21}$ cm^{-3} is the critical electron density. A more massive outer sublayer allows to increase the target explosion time. The target is considered as a fully ionized plasma, one ion and 79 electrons per cell, with the initial electron temperature 100 eV. This high initial temperature is chosen due to the computational restrictions. Though it may lead to

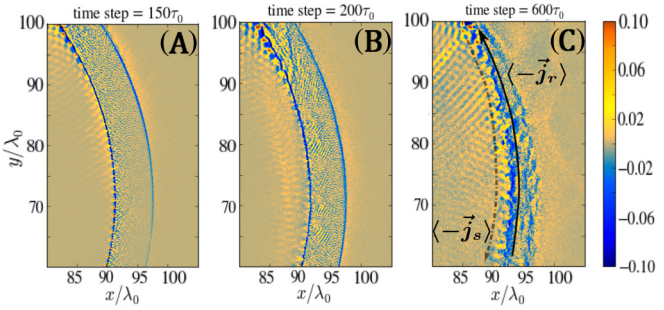

FIG. 2. (Color online) Current density j_y in the selected domain marked with a dashed lines in Fig. 1(A2,B2), in subsequent time moments 0.46,0.62,1.9 ps. Negative, more intense current is responsible for a negative B_z in Fig. 1(A2,B2,C2,D2). In (C) the dot-dashed arrow shows electrons, directly accelerated by the laser pulse, the solid arrow shows electrons, which produce the inverse current.

the underestimation of collisions at the initial interaction stage, it should not play an important role after electrons are heated by the laser pulse. The simulation box is 2160 × 2304 cells, or approximately 100 × 110 μm. The resolution time is 0.16 fs.

Although the target density in our simulation is lower than the real solid density, we expect a qualitatively correct description of the main physical processes inside the bulk of the target. This confidence is based on our choice of the interaction regime with a highly overcritical plasma and on taking into account the electron collisions. For that we implemented a fully relativistic binary-collision model, operating with the real solid density, set as an additional parameter. The model is based on Takizuka and Abe model [13], which features a perfect energy conservation in individual collisions and a momentum conservation on the average, with the specifics coming out from the use of weighted particles [14]. The model we use reproduces well the analytical exchange rate and describes fast electron stopping in dense plasmas in agreement with the NIST database. To test the effect of collisions and the density of the target material, and so to prove the robustness of the proposed 'escargot' setup, several simulations were carried out with different materials and different model-to-real density ratios. In all these simulations we observed the same physical processes and similar values of the generated magnetic fields.

Several subsequent snapshots of the electron density (A1–D1) and magnetic field B_z (A2-D2) during the interaction process are shown in Fig. 1. Even though a large part of the laser energy is absorbed by the target, the laser radiation follows the geometry of the 'escargot' chamber, which works as a plasma mirror of a specified form. To reveal the origin of the magnetic fields, the current structure is shown in Fig. 2. The total current near the target surface is composed of the electrons, accelerated by the surface guiding mechanism [6], which are moving along the surface, and of the return current, generated in the target in order to compensate the charge accumulation caused by escaped electrons. This total current produces B_z magnetic field, which affects the electron dynamics. In the upper part of the target (∼0°–10°), where the laser propagation is almost grazing, the surface guiding effect is most important. Below, in the main region of the laser pulse reflection, the incident angle increases up to ∼40°–45°. Under

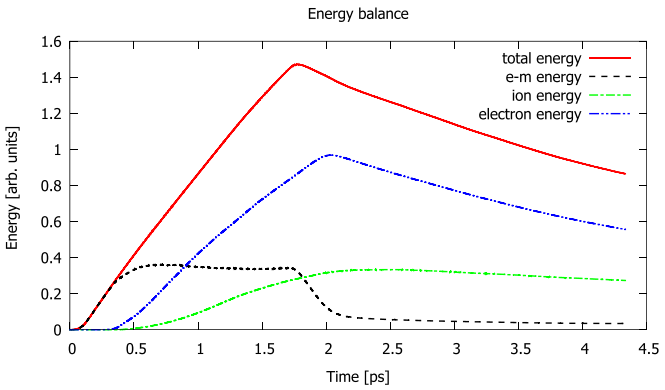

FIG. 3. (Color online) Energy balance during the interaction. After 2 ps, when the laser pulse is gone, the electromagnetic energy is composed only by the magnetic field energy, which has the order of 5–7 % of the total laser pulse energy.

these conditions the surface guiding mechanism still works [6], and the corresponding direct current is seen in Fig. 2(A) as a thin layer of positive current along the surface. The inverse current (negative in Fig. 2), appears to be more stable and possesses a higher value in comparison to the direct one. While the laser pulse propagates further, it heats more electrons near the inner surface of the target. These electrons escape the target thus creating a local positive charge. This is the nature of a *return current feeding* by the laser propagation along a curved target surface. The direction and the amplitude of the magnetic field inside the cavity is defined by the total current distribution, as it is discussed below. Note that the resulting magnetic structure possesses a θ-pinch-like geometry, which is known to be stable, and thus its lifetime is defined generally by the target life time. Later on, see Fig. 1(C1,C2), the Target Normal Sheath Acceleration (TNSA) mechanism [15] of ion acceleration comes into play, pulling ions from the target inner surface into the target void. This effect lately leads to an additional compression of the magnetic field by the plasma pressure.

The energy conversion efficiency from the laser to the remaining magnetic field may be estimated from the energy balance in the PIC simulations shown in Fig. 3. The total energy growth is approximately linear during the time when the laser pulse is on, and after it ends, the energy gradually decreases, because the most energetic particles leave the simulation box. Initially, the electromagnetic energy also grows linearly, but approximately at 0.4 ps, when the laser reaches the target, its growth stops due to the electron heating. On the contrary, during the laser interaction with the target, the electron energy grows, reaching the value of the order of ≈60% of the total energy at the end of the laser pulse. Also a significant part of the total energy is transmitted to ions due to the TNSA effect. The electromagnetic energy remains of the same level of ≈35% of the total laser energy during the laser-target interaction process, but when the laser pulse ends it does not decrease to zero. The remaining part, left after 2 ps, corresponds to the energy of the residual magnetic field. According to Fig. 3 this magnetic field contains about 5–7 % of the total laser pulse energy.

III. DISCUSSION

The magnetic field evolution consists of several subsequent processes. These are the electron heating by the laser pulse, currents generation, magnetic structure formation, and TNSA effect. We discuss first the current structure and estimate the corresponding magnetic fields. Although the main role in the magnetic field generation is played by the reverse current, the direct electron current along the target inner surface is also important. To estimate the magnetic field amplitude, Ampère's law may be used:

$$\vec{\nabla} \times \vec{B} = \frac{4\pi}{c}\vec{j} + \frac{1}{c}\frac{\partial \vec{E}}{\partial t}, \tag{2}$$

where $\vec{B}$ and $\vec{E}$ are magnetic and electric fields, $\vec{j}$ is a current, and c is the light velocity. To estimate the quasi-static magnetic field we average Eq. (2) over time τ_{av}, which is much longer than both the laser period $\tau_{av} \gg \omega^{-1}$ and the electron plasma period $\tau_{av} \gg \omega_e^{-1}$. After this, the displacement current $\langle \partial \vec{E}/\partial t \rangle$ in Eq. (2) becomes very small and can be omitted. This means, that the average currents $\langle \vec{j} \rangle$ form a self-consistent structure with the magnetic fields $\langle \vec{B} \rangle$, and that the fast varying electric field responsible for electron heating on the inner target surface does not contribute much to the quasi-static $\langle \vec{B} \rangle$ generation. According to the current structure shown in Fig. 2(C), it is important to consider both the direct surface current $\langle \vec{j}_s \rangle$ and the reverse one $\langle \vec{j}_r \rangle$. It is convenient first to estimate the total number of the escaping electrons from the surface and their average energy.

For relativistic laser intensities, the characteristic electron energy T_e is defined by the ponderomotive scaling [16]. For $I_0 = 5 \times 10^{19}$ W/cm^2 gives $T_e \sim 4$ MeV, which is consistent with the simulation. The number of escaped electrons in a stationary regime N_{esc} can be found from the self-consistent solution of the Poisson-Boltzmann problem [17], which gives for the focal radius $r_f \sim 10\,\mu$m, $N_{esc} \sim 6 \times 10^{12}$ electrons. This number gives the total electric charge and the return current $\langle \vec{j}_r \rangle$, in the the target during the laser pulse time τ_0. According to the numerical simulation, the number of electrons near the surface, participating in the current $\langle \vec{j}_s \rangle$ is about $\kappa \sim 0.1$–$0.2 \lesssim 1$ of the total electron number N_{esc} for moderate oblique angles [6]. According to these estimates supported by Fig. 2, the scale of the current density is about 0.1 in relativistic units. The return current $\langle \vec{j}_r \rangle$ is a part of the total electron current composed by $\langle \vec{j}_s \rangle$, $\langle \vec{j}_r \rangle$, and $\langle \vec{j}_3 \rangle$, indicated in Fig. 1(B2) with the long-dashed arrow. The magnetic field near the target surface may be estimated from Eq. (2), as $\partial \langle B_z \rangle / \partial x \approx 4\pi/c \cdot \langle j_y \rangle$, where $\langle j_y \rangle$ is a projection of the electron current on the y axis. Here, $\langle j_y \rangle$, near the inner surface consists of the y-projections of the direct current $\langle \vec{j}_s \rangle$ and the return current $\langle \vec{j}_r \rangle$, both of the order of 0.1, though $\langle j_s \rangle < \langle j_r \rangle$, see Fig. 2. According to these values, the magnetic field at the spatial scale ~ 1 is of the order of 2.5 relativistic units, or ≈ 300 MG (compared to the values in Fig. 1). The magnetic field appears to be frozen into the expanding plasma, which propagates gradually to the center of the target cavity, and fills it with the magnetic field, as is shown in Fig. 1.

When the magnetic field is formed, the electrons which form the surface current $\langle \vec{j}_s \rangle$, as well as other fast electrons

from the irradiated region, may be deflected in it. The Larmor radius for electrons with an energy of 4 MeV in a magnetic field seen in Fig. 1(B2), ∼200 MG, is much smaller than the target size: $r_L \lesssim 1$ μm. This means, that these electrons cannot penetrate into the magnetized region. However, they can propagate along the edge of the strongly magnetized region, and form the third current $\langle \vec{j}_3 \rangle$. In the given geometry, these electrons propagate approximately through the middle of the inner target void, separating it and forming a bipolar magnetic field distribution. Variation of the $\delta r/r_0$ parameter in Eq. (1) and the laser propagation direction may affect the shape of the magnetic field structure: for a large $\delta r/r_0$, the current $-\langle \vec{j}_3 \rangle$ is ejected outside the cavity and the generated magnetic field may take an unipolar shape. The shape is also time-evolving at the time scale of tens of picoseconds, see Supplemental Materials [9] and [12].

The generated longitudinal magnetic structure lives after the end of the laser pulse, before the target explodes. Moreover, during this stage we observe an interesting effect of a magnetic field compression by the plasma expansion inside the cavity. This process has a time scale much greater than the kinetic and magnetic plasma characteristic times, and may be qualitatively described by the pressure balance between the magnetic field and the hot plasma. From Fig. 1, where the separation between strongly magnetized low-density and low-magnetized high-density plasmas is quite thin, we estimate the electron density inside this boundary as $n_e \sim 0.5 \times 10^{21}$ cm^{-3}. Taking the electron mean energy from the ponderomotive scaling $T_e \sim$ 4 MeV, we obtain from the balance relation

$$\frac{B_z^2}{8\pi} \approx n_e T_e, \tag{3}$$

the magnetic field value $B_z \sim 200$ MG, in a good agreement with Fig. 1. Note, that the relation (3) is usual for θ-pinch configurations, where a magnetized plasma with a spatially distributed density is confined in a magnetic field.

At these times, inside the target cavity we observe an interaction of a low-density hot magnetized plasma [the blue (dark) region with a negative $\langle B_z \rangle$ in Fig. 1(C2,D2)] and a more dense cold magnetized plasma [the yellow (bright) region with a positive $\langle B_z \rangle$ in Fig. 1(C2,D2)]. A low-density plasma region is formed along the more heated right part of the target. There a dense hot collisionless surface plasma cannot be rapidly magnetized and remains for some time separated from the magnetized region. In the left part of the target, plasma is relatively cold, but the magnetic field, generated by the current $\langle \vec{j}_3 \rangle$ is strong. There a considerable part of the surface plasma may be magnetized, see Fig. 1(C1,C2). Finally, the ablated plasma comes to an equilibrium (3) with the magnetic field inside the cavity. The time evolution of this quasi-static stage is defined mainly by the target explosion time, so that more dense materials may be preferable to increase the life time of the generated magnetic structure.

IV. CONCLUSIONS AND PERSPECTIVES

We presented two-dimensional calculations of a strong quasistationary magnetic field generation with intense laser pulses. For a possible experimental realization, the question of the role of 3D effects arises. The θ-pinch type magnetic structure, observed in our simulations, is expected to be stable at the time scale of at least tens of ps [12]. The required laser intensity of 5×10^{19} W/cm^2 and the pulse duration of 1.6 ps could be achieved with the laser energy of the order of 1 kJ. This is the scale of installations such as PETAL, ORION, OMEGA EP, and LFEX.

The laser contrast is worthy of a discussion in the considered scheme. Because of the unique geometry, our target provides a high absorption due to the confinement of the laser pulse, even without a preplasma. That means that the laser energy is trapped in the 'escargot' target cavity and such a 'black body' radiation defines the plasma temperature. In the above Gold-type example we considered a target without preplasma, which corresponds to a laser pulse with a high contrast $\lesssim 10^{-8--10}$. However, we examined also targets with preplasma, like the Al-type target, see Supplemental Material [12], and found that the mechanism we describe remains efficient in this case.

The robustness of the considered mechanism of magnetic fields generation was confirmed in several runs with different target and laser parameters. To be more convincing, we present in details the results of another simulation for an aluminum-type target with a preplasma, see Supplemental Material [12]. The results for the two targets, the Gold-type one, described in details above (for the time evolution see Supplemental Material [9]), and Al-type target (see Supplemental Material [12]), have both ion densities smaller than the real solid ion density, which is a tribute to numerical limitations; however, the Al-type target has ion density approximately 30 times greater, than that in the gold-type target. The generated magnetic field strength in these two cases has approximately the same value. This confirms that electrons play the main role in our conditions of a relativistically intense laser pulse interacting with an over-dense plasma at a ps time scale.

As we found, a strong return current in a predefined target geometry can be a flexible and effective experimental tool. It is known [17], that return currents depend strongly on the experimental realization, including a holder position on the target. For the considered 'escargot' setup, we marked a possible 'support point', which should not strongly affect the current distribution during the interaction. The proposed scheme for the magnetic field generation may be used in a variety of applications, such as laboratory astrophysics experiments, neutron production, different aspects of ICF, i.e., electron magnetic collimation [18], etc. Several possible variations, which present generalizations of the considered above 2D model to the 3D case, are presented in Fig. 4. In these examples, targets should possess the same properties as the described above for a 2D 'escargot' target. Namely, they are to be produced of a heavy material to increase the lifetime, the spatial scale should be adjusted to get the maximum energy deposition inside the target cavity, and a holder in each case should be placed so that the return current can be generated along the whole laser-irradiated surface.

In laboratory astrophysics applications, a magnetized plasma may be used for the studies of collisionless shocks and magnetic reconnection phenomena [19]. Depending on laser and target parameters it may be possible to create magnetized plasmas, propagating in the opposite directions, with different orientations of the magnetic field. This can avoid magnetic compression [20], which is considered as not a typical effect in space plasmas. A possible setup for the reconnection studies

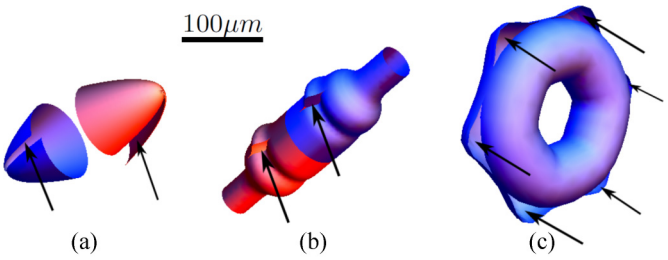

FIG. 4. (Color online) Examples of target geometries for the experimental applications of the considered effect: (a) Two cone-like 'escargot' targets for collisions of magnetized plasmas; (b) magnetic trap geometry; (c) microtocamak geometry. Black arrows show laser pulses directions.

is shown in Fig. 4 a. Inside a single 'escargot' target (1), with adjusted laser and target parameters, reconnection phenomena may also take place, as it follows from the structure of the magnetic field in Fig. 1. Another application may be found with micrometer-scale magnetic traps, shown in Figs. 4(b) and 4(c). Target sizes and magnetic field values may be of the order of interest for neutron production or magnetized fusion schemes [21]. For the magnetic field $\langle B \rangle \approx 100$ MG, and the trap radius about 50 μm, it can confine protons with energies $\sim$30 MeV, and α particles with energies of the order of $\sim$10 MeV.

In conclusion, a novel scheme of laser-assisted production of intense magnetic fields is proposed. In comparison with the actual setups, it allows to increase the amplitude of the magnetic field at least an order of magnitude. The generated field is localized in a spatial region of several tens of microns, and its lifetime is defined by the hydrodynamic time of disassembly of the irradiated target. The scheme is based on the generation of the intense currents, which propagate along the curved surface. As a first "proof-of-principle" example, with the 'escargot'-like target we demonstrated a simple quasi-static θ-pinch type magnetic structure. More complex magnetic field micro-structures may be produced with more complicated target geometries.

ACKNOWLEDGMENTS

Authors greatly appreciate useful discussions with S. Fujioka, A. Poyé and J. J. Santos. The work is in part supported by the French National funding agency ANR within the project SILAMPA, and it was granted access to the HPC resources of CINES under the allocations 2014-056129, 2015-056129 made by GENCI (Grand Equipement National de Calcul Intensif), and of MCIA of the Bordeaux University. This work was supported by the Russian Presidential Grants for the Support of the Leading Scientific Schools (project no. NSh-4829.2014.2). This work has been carried out within the framework of the EUROfusion Consortium and has received funding from the European Union's Horizon 2020 research and innovation program under grant agreement no. 633053.

[1] D. Ryutov, Astrophysics and Space Science **336**, 21 (2011).
[2] S. Fujioka *et al.*, Scientific Reports **3**, 1170 (2013).
[3] H. Yoneda, T. Namiki, A. Nishida, R. Kodama, Y. Sakawa, Y. Kuramitsu, T. Morita, K. Nishio, and T. Ide, Phys. Rev. Lett. **109**, 125004 (2012).
[4] P. Korneev, E. d'Humieres, and V. Tikhonchuk, arXiv:1409.5246 (2014).
[5] P. Korneev, E. d'Humieres, and V. Tikhonchuk, arXiv:1410.0053 (2014).
[6] T. Nakamura, S. Kato, H. Nagatomo, and K. Mima, Phys. Rev. Lett. **93**, 265002 (2004); T. Nakamura, K. Mima, H. Sakagami, and T. Johzaki, Phys. Plasmas **14**, 053112 (2007).
[7] Y. T. Li *et al.*, Phys. Rev. Lett. **96**, 165003 (2006).
[8] J. Psikal, V. T. Tikhonchuk, J. Limpouch, and O. Klimo, Physics of Plasmas (1994–present) **17**, 013102 (2010).
[9] See Supplemental Material at http://link.aps.org/supplemental/10.1103/PhysRevE.91.043107 for the time-dependent behavior of the electron density and the magnetic field in the Gold-type target.
[10] G. A. Mourou, T. Tajima, and S. V. Bulanov, Rev. Mod. Phys. **78**, 309 (2006).
[11] Y. Sentoku and A. J. Kemp, J. Comput. Phys. **227**, 6846 (2008).
[12] See Supplemental Material at http://link.aps.org/supplemental/10.1103/PhysRevE.91.043107 for the time-dependent behavior of the electron density and the magnetic field, and the energy balance in an Al-type target.
[13] T. Takizuka and H. Abe, J. Comp. Phys. **25**, 205 (1977).
[14] K. Nanbu and S. Yonemura, Journal of Computational Physics **145**, 639 (1998).
[15] P. Mora, Phys. Rev. Lett. **90**, 185002 (2003).
[16] S. C. Wilks, W. L. Kruer, M. Tabak, and A. B. Langdon, Phys. Rev. Lett. **69**, 1383 (1992).
[17] A. Poyé *et al.*, Phys. Rev. E **91**, 043106 (2015); J.-L. Dubois *et al.*, *ibid.* **89**, 013102 (2014).
[18] F. Pérez *et al.*, Phys. Rev. Lett. **107**, 065004 (2011).
[19] M. Yamada, R. Kulsrud, and H. Ji, Rev. Mod. Phys. **82**, 603 (2010).
[20] P. Korneev, E. d'Humières, and V. Tikhonchuk, Phys. Plasmas (1994–present) **21**, 022117 (2014).
[21] A. Hasegawa, H. Daido, M. Fujita, K. Mima, M. Murakami, S. Nakai, K. Nishihara, K. Terai, and C. Yamanaka, Phys. Rev. Lett. **56**, 139 (1986).